# Mechanism of Photoinduced Bending and Twisting in Crystalline Microneedles and Microribbons Composed of 9-Methylanthracene

Taehyung Kim, Lingchao Zhu, Leonard J. Mueller, and Christopher J. Bardeen*

Department of Chemistry, University of California, Riverside, California 92521, United States

Ⓢ Supporting Information

ABSTRACT: The solid-state photodimerization of 9-methylanthracene is used as a model system to investigate how crystal morphology and reaction dynamics affect photomechanical deformations of single microcrystals. By varying the crystallization conditions, two different crystal shapes, microneedles and microribbons, are grown on a clean water surface. The microribbons twist under irradiation, while the microneedles bend. In both shapes, the maximum deformation occurs at roughly the midpoint of the reaction, while further dimerization causes the crystals return to their original shapes. Powder X-ray diffraction patterns establish that the needles and ribbons have the same crystal orientation and that the photoreaction proceeds in a crystal-to-crystal manner. NMR spin−lattice relaxation measurements are consistent with the rapid formation of large (>100 nm) dimer crystal domains. Simultaneous measurement of the needle bending and monomer fluorescence signal allows us to correlate the bending with the reaction progress. The behavior is qualitatively reproduced by a model in which the motion is driven by strain between spatially distinct reactant and product domains, also called heterometry. We consider several different mechanisms that could give rise to these spatially distinct domains. The ability to control the photoinduced crystal deformation by manipulating crystal shape and solid-state reaction kinetics suggests that photoreactive molecular crystals may be useful for generating well-defined motions on small length scales.
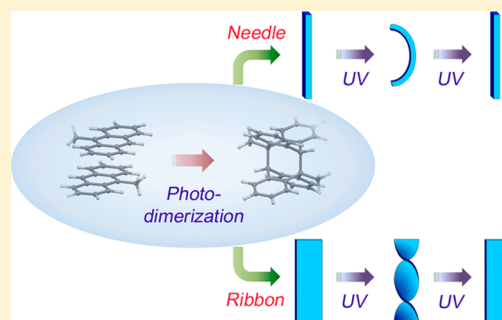
INTRODUCTION

In solid-state photochemistry, the geometrical constraints of the surrounding medium can have a profound effect on the reactivity of the molecule.[1−3] Schmidt and co-workers pioneered the systematic study of how crystal structure influences molecular reactivity, a field of study broadly defined as topochemistry.[4,5] But while crystal packing has long been known to affect the ability of a molecule to undergo a photochemical reaction, it is also true that the photoreaction can drive changes in the crystal structure. Such changes manifest themselves on the molecular scale as changes in the packing of the product molecules. On the macroscopic scale, when a molecular crystal begins to react, it becomes a heterogeneous mixture of reactant and product domains, with a buildup of strain forces at the interfacial regions. Often, the interfacial strain is sufficient to fracture the crystal, leading to disintegration.[6] But there are also examples of molecular crystal systems that remain intact while the internal photochemistry changes their shapes on micrometer or larger length scales. Photomechanical actuation in several different classes of photochromic molecular crystals has been observed by multiple research groups,[7−17] with Irie and co-workers showing that such systems can be remarkably robust and reversible.[18,19] Such crystals may have practical applications as photomechanical actuators.

The present challenge is to develop strategies to engineer the mechanical response of these molecular crystals. One approach is to control illumination conditions, for example making crystals bend in response to illumination from one side. Asymmetric illumination conditions give rise to an asymmetric distribution of products and reactants, e.g., a layer of photoproduct molecules on the side closest to the light source. The resulting gradient of reacted and unreacted molecules forms a bimorph structure, where the interfacial strain between the two phases drives the mechanical distortion, most often bending.[20] This mechanism is used in many polymer-based materials as well.[21] While straightforward for large crystals, this approach becomes impractical once the crystal dimensions approach the diffraction limit of the exciting light. The capability to generate controlled motion in ultrasmall molecular crystals is an important goal, since they could function as actuators in devices on the length scale of biological cells. Submicrometer molecular crystals also have the advantage of being more resistant to fracture.[7,22,23]

An important question in the field is whether asymmetric illumination conditions are necessary to generate directional motion. In recent work, we observed that nondirectional illumination by ultraviolet (UV) light induces twisting in crystalline microribbons composed of 9-anthracene carboxylic acid (9AC) and 4-chloro-cinnamic acid (4Cl-CA).[24,25] These motions result from [4+4] and [2+2] photodimerization

reactions, respectively. In the case of 9AC, this twisting was reversible thanks to the metastable nature of the photodimer. We attributed the twisting to the creation of a heterogeneous mix of monomer and photodimer where interfacial strain between the two phases provided the deformation energy. Both of these molecules crystallize in one-dimensional hydrogen-bonded stacks where statistical considerations prevent the photodimerization from going to 100% conversion.[26] Both systems also have transient photoproducts: the [4+4] 9AC dimer reverts back to monomer within a few minutes, while the [2+2] 4Cl-CA dimer crystal decomposes into an amorphous phase within a few hours. In neither case were we able to characterize the twisted structure in detail. Basic questions, like whether heterogeneous domains of reactant and product form within the crystal, could not be answered. If a bimorph type of structure can be spontaneously formed without the use of special illumination conditions, then it becomes more likely that photomechanical actuators can be scaled down to the nanoscale level.

To investigate the origin of the directional motion, in this paper we turn to the solid-state [4+4] photodimerization reaction of 9-methylanthracene (9MA), an anthracene derivative whose photochemistry has been characterized in solution and in the solid state.[27−32] This molecule crystallizes in a herringbone pair motif (Figure 1) where every anthracene is
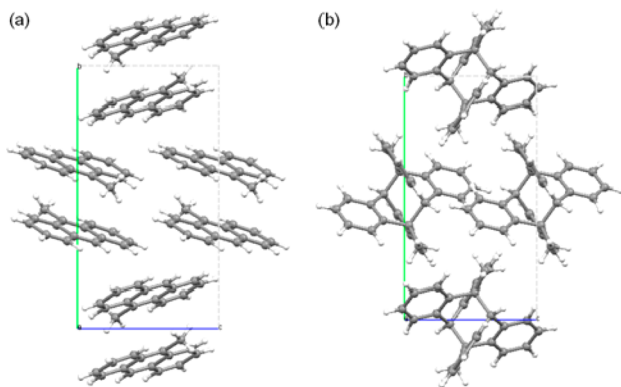

Figure 1. Crystal structures of 9MA monomer (a) and dimer (b) viewed along the direction of *a*-axis of the unit cell. Structures taken from ref 31.

paired with a partner, allowing the photoreaction to proceed to 100% completion, at least in principle. The dimerization can be reversed by heating or 254 nm light,[33−35] but under ambient conditions the crystalline photodimer is stable, and the reaction is effectively irreversible. The 9MA system thus provides an opportunity to characterize crystals over the entire course of their photomechanical response, controlling the fraction of reacted 9MA molecules by varying the duration of light exposure. In this Article, we examine how different microcrystal growth conditions lead to different 9MA crystal shapes, which in turn lead to different types of photoinduced motions. We then use multiple characterization techniques [powder X-ray diffraction (PXRD), solid-state nuclear magnetic resonance (SSNMR), and fluorescence microscopy] to map out the photoreaction dynamics and domain formation. Using time-resolved fluorescence microscopy, we examine how the deformation of a 9MA crystal microneedle evolves from straight to bent and finally back to straight again as the monomer → dimer reaction proceeds under light exposure. A

model based on an exponential distribution of dimer product, leading to an effective bimorph structure, does a good job of qualitatively reproducing the data. The ability to produce such a structure in a photoreactive molecular crystal under uniform illumination provides motivation for the design of smaller photomechanical structures. The irreversibility of the 9MA photodimerization makes it an unlikely candidate for practical photomechanical applications. It is, however, an ideal model system to illustrate how heterogeneous reaction kinetics and crystal shape can be used as design elements for the development of new photomechanical materials.

■ EXPERIMENTAL SECTION

1. Preparation of 9MA Microneedles and Microribbons. 9MA microneedles were prepared using the floating drop method. First, 1.1 mL of 9MA (Alfa Aesar, 99%) solution in hexanes (Fisher Chemical, 99.9%) with 1.9 mg/mL concentration was slowly added onto the surface of Milli-Q purified water (Millipore) in a 60 × 15 mm Petri dish. A glass cover was placed on the Petri dish, and it was stored for 24−48 h without being exposed to light. Slow evaporation of the solvent left needle-shaped crystals on the water surface. 9MA microribbons were prepared using the same process but with 1.0 mL of 1.9 mg/mL 9MA solution in xylenes (Fisher Chemical, >98.5%) and evaporation occurring over the course of 1 week.

2. Characterization. *2.1. Scanning Electron Microscopy (SEM).* Floating microribbons or microneedles were transferred onto an Anodisc membrane (Whatman Co., 13 mm diameter, 0.2 μm pore size). After drying, the sample was coated with Pt/Pd in a Sputter coater (Cressington 108 Auto), and observed using a FEI-Philips XL-30 FEG scanning electron microscope.

2.2. Optical Microscopy. After microcrystals were prepared on the water surface, a few drops of 50% H_3PO_4 were added to the water to prevent evaporation during microscopic observation. The acidic suspension of microcrystals was dropped onto a microscope glass slide and covered with a coverslip. The crystal twisting and bending behaviors after exposure to 365 nm UV light were observed using an Olympus IX70 inverted microscope equipped with a DCM-300 digital camera. Simultaneous observation of microneedle bending and its fluorescence signal was accomplished by using a glass coverslip as a beamsplitter in front of the digital camera to divert part of the fluorescence into a photomultiplier tube (Hamamatsu) with a 550 nm interference filter attached. The rest of the fluorescence passed through the coverslip to be imaged by the digital camera.

2.3. Powder X-ray Diffraction. All XRD data were collected on a Bruker D8 Advance X-ray powder diffractometer (CuK radiation, λ= 1.5418 Å, 40 kV/40 mA power) at room temperature. Samples for XRD of flat 9MA microcrystals were prepared by dropping a suspension of microcrystals on a glass slide and carefully wicking away the excess water using a Kimwipe tissue.

2.4. ^{13}C Solid-State Nuclear Magnetic Resonance. Cross-polarization (CP) magic-angle-spinning (MAS) SSNMR experiments were performed at 14.1 T (^1H frequency 600 MHz) on a Bruker AVANCE spectrometer equipped with a double-resonance 4 mm MAS probe, spinning at a MAS rate of 8 kHz. The MAS spin rate of 8 kHz was chosen to place the majority of the upfield resonances between the first and second order spinning sidebands of the monomer and dimer aromatic peaks. 83 kHz ^1H $\pi/2$ and decoupling pulses (SPINAL64)[36] were used along with a 2 ms CP spin-lock. During CP the ^1H nutation rate was set to 50 kHz and the ^{13}C nutation rate ramped from 37 to 46 kHz. For each spectrum, 4096 complex data points with a dwell of 10 μs (spectral width 50 kHz, total acquisition time 41.01 ms) were acquired, with a typical recycle delay of 240 s. In all, 256 transients were coadded, for a total experiment time of 17 h and 20 min. All experiments were performed at room temperature and referenced to TMS via an external adamantane standard (downfield peak set to 38.48 ppm).

^1H T_1's were measured indirectly by varying the relaxation delay in the cross-polarization experiment. As the proton magnetization is

saturated by decoupling during ^{13}C detection, it recovers exponentially, with the proton T_1 value encoded in the ^{13}C intensity after cross-polarization. Delay values from 1 to 1000 s were typically employed with 256 transients acquired at each delay point. These experiments were performed at 10.5 kHz in order to move the second-order spinning sidebands off the dimer methyl peak.

Solid 9MA samples for CPMAS studies were prepared by spreading microcrystals across a glass microscope slide and irradiating with a 365 nm Mercury lamp in air. After irradiation, the crystals were swept into the 4 mm diameter zirconia MAS rotor. No tangible differences in either the chemical shifts or T_1 recovery profiles were discerned between random microcrystals and microneedles grown using the floating drop method with hexanes.

■ RESULTS

1. Preparation and Characterization of Microcrystals.
We used the floating drop method to grow crystalline microribbons and microneedles of 9MA from various solvents on a clean water surface. In general, we had more difficulty growing ribbons of 9MA than we did with a previously studied molecule, 9AC. We attribute this to the different crystal structures (9AC has a natural one-dimensional stacking motif)[37] and to the greater hydrophobicity of 9MA, which makes it more resistant to spreading on the water surface. Nevertheless, we were able to find conditions where we could reproducibly grow microcrystals with reasonably well-defined morphologies. Using hexanes, we could grow crystals with rectangular cross sections where the aspect ratio (width w to height h) ranged from 1 to 3. A representative SEM image of these crystals, which we refer to as "microneedles" is shown in Figure 2a. Also shown is a histogram of the aspect ratios for
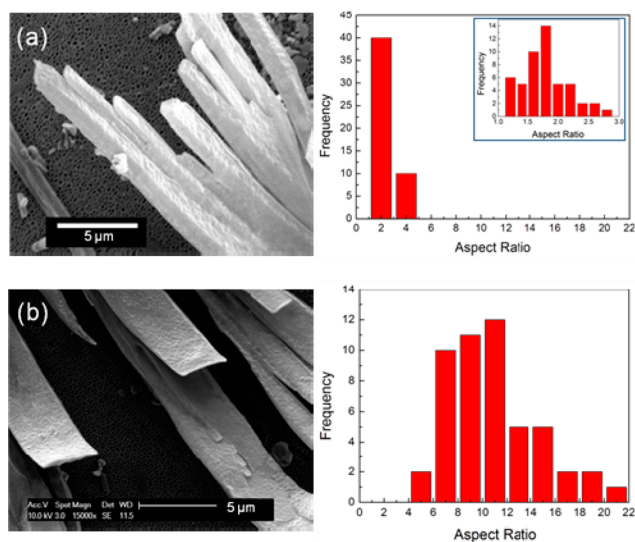

Figure 2. SEM and histogram analyses of (a) 9MA microneedles and (b) 9MA microribbons. The inset of (a) shows an enlarged histogram with a narrower bin size to show the aspect ratio of the 9MA microneedles in more detail.

individual microneedles determined by end-on SEM imaging, as described in the Supporting Information. When a different solvent, xylenes, was used, the aspect ratio increased by almost a factor of 10, and we term these crystals "microribbons". A SEM image and histogram for these crystals are shown in Figure 2b. The tendency of xylenes to promote the growth of wide, flat single crystals has been noted previously in the case of anthracene[38] and attributed to its relatively large spreading

coefficient on water. But we should emphasize that the growth of well-defined single needles and ribbons only occurs within a narrow range (±10%) of 9MA concentrations and that the final distribution of crystal shapes is likely a complex function of nucleation kinetics (influenced by the solute concentration and solvent evaporation rate) and solvent properties (surface tension, spreading coefficient and solubility). We were not able to derive simple rules that govern whether crystals with a specific aspect ratio would be formed in a particular solvent.

The oriented, single-crystal nature of the needles and ribbons was confirmed by PXRD measurements. Using the same methods employed previously for 9AC microribbons,[24] we measured the PXRD pattern for 9MA ribbons and needles lying flat on a glass substrate. As shown in Figure 3a, in both cases
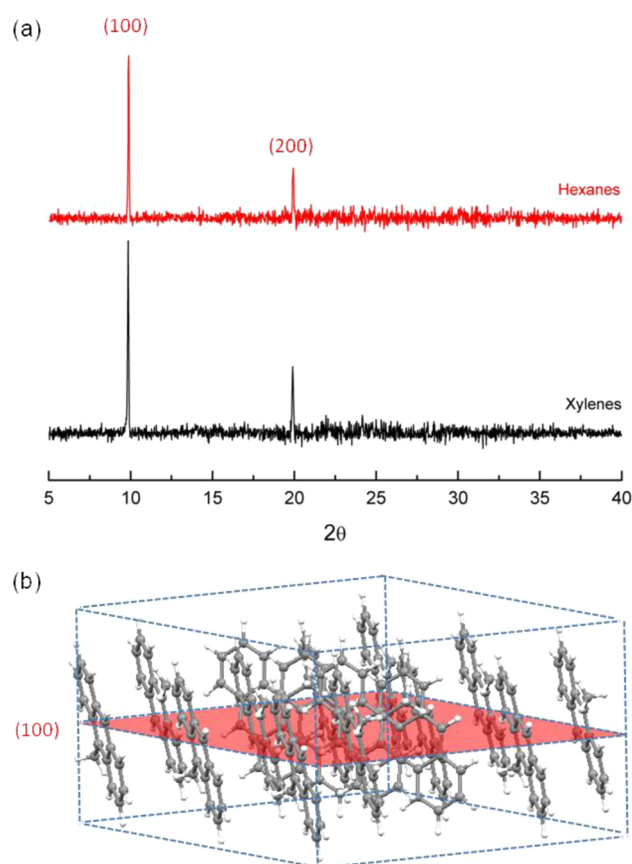

Figure 3. (a) PXRD pattern of 9MA microneedles (red trace, prepared from hexanes) and microribbons (black trace, prepared from xylenes) lying flat on a glass slide. These patterns can be compared to that of an unoriented 9MA powder that is shown in Figure 5. The appearance of only two diffraction peaks from the parallel Miller (100) and (200) planes indicates that the differently shaped crystals have similar orientations. (b) Crystal packing of 9MA molecules within microneedles and microribbons, showing the (100) Miller plane.

only diffraction peaks corresponding to the (100) and (200) Miller planes were observed. These two planes are parallel to each other and must also be parallel to the substrate (i.e., perpendicular to the height axis h) in order to generate substantial diffraction intensity. The crystal orientation deduced from this measurement is shown in Figure 3b. The herringbone pairs form a plane parallel to the width and length of the ribbons. We note that this layer of herringbone pairs lies in the bc crystal plane for both the monomer and dimer crystals.

When they undergo photodimerization, one would expect substantial volume changes along these directions.

2. Solid-State Photoreaction Characterization. When the needles and ribbons are exposed to 365 nm UV irradiation ($\sim$100 mW/cm^2) from a mercury lamp in a fluorescence microscope, the green excimer fluorescence (500−600 nm) of the 9MA crystal rapidly fades, leaving a much fainter blue fluorescence (400−500 nm) that we ascribe to unreacted 9MA monomers. The loss of the excimer fluorescence is accompanied by large shape changes in both types of crystals. The needles undergo a bending motion during irradiation, but then return to their original shape as time goes on. An example of this shape evolution is given in Figure 4a. The net shape change
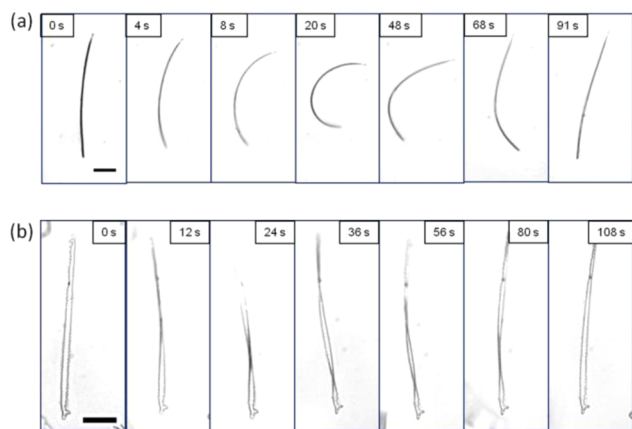

Figure 4. Optical microscope images of bending and unbending of a 9MA microneedle (a) and twisting and untwisting of a 9MA microribbon (b) during 365 nm UV irradiation. Scale bars: 20 μm.

after a long period of irradiation is very small, but at intermediate times the needle is highly deformed. A similar sequence of events is observed for the microribbons composed of 9MA, as shown in Figure 4b. Before illumination, the ribbon is flat and straight. Under illumination, the ribbon twists but as the photoreaction proceeds, it straightens out again and returns to close to its original shape. The photoinduced twisting seen for the 9MA ribbons is similar to what we previously observed for 9AC ribbons, but in 9MA the untwisting results from the continuing photoreaction, rather than a spontaneous back-reaction that occurs after the light is turned off. The two most important observations are that (1) the type of photo-mechanical deformation (bend versus twist) depends on the shape of the crystal, even though the crystal orientation and packing are identical, and (2) the deformation is maximized at intermediate stages during the photoreaction, while at the end point the crystal has returned to its original shape. We also note that these microcrystals remain intact, in contrast to the large structural disruptions seen in larger 9MA crystals after irradiation.[30]

The images in Figure 4 clearly show that the internal photochemical reactions can drive large scale shape changes. To characterize the photochemical reaction in more detail, we turned to XRD and NMR spectroscopy experiments. The first question is whether the 9MA photoreaction is a crystal-to-crystal reaction. Early single-crystal XRD work by Turowska-Tyrk indicated that this reaction did proceed in a crystal-to-crystal fashion, although she was unable to follow the reaction to completion due to the disintegration of her single crystals at high conversion.[31] By performing PXRD measurements on

microcrystalline powders of 9MA, we have confirmed that reaction of the 9MA monomer crystal yields crystalline 9MA dimer, as observed by previous workers.[32] In Figure 5 we show
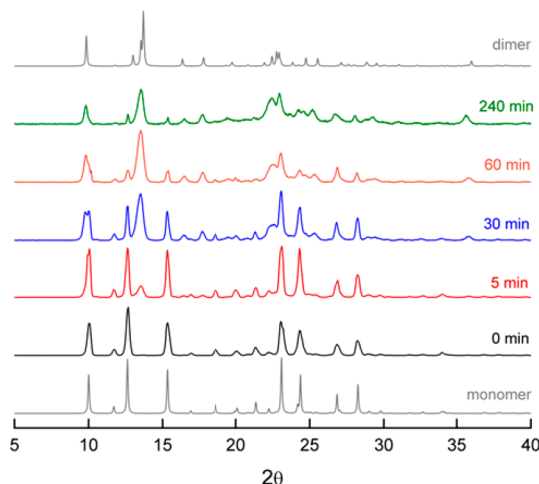

Figure 5. PXRD data of 9MA microcrystals under 365 nm UV exposure for 0, 5, 30, 60, and 240 min. The data can be compared to the calculated patterns of monomer (bottom) and dimer crystals (top).

a series of PXRD measurements and compare them with theoretical powder patterns derived from the known crystal structures of 9MA monomer and dimer.[31] Comparison of the unreacted monomer PXRD pattern with the calculated pattern shows a good correspondence between the peak positions and relative intensities. The peak broadening seen in the experimental data is due to the instrument resolution. As the monomer crystal is exposed to UV radiation, the monomer peaks decrease while new peaks begin to appear, notably at 2θ = 9°, 13°, and 36°. After 4 h of exposure, it can be seen that the PXRD pattern is dominated by the dimer crystal pattern, whose calculated shape is shown at the top of the figure. There is still a trace of the monomer crystal left, however, as can be seen most easily seen by the surviving peak intensity at 2θ = 16° and 28°. These data show that photodimerization of the monomer crystal leads to the formation of dimer crystals, and that both crystal phases are present during the reaction. From the PXRD data, the 9MA dimerization appears to be a clean solid-state photoreaction, with no sign of the metastable crystal intermediates observed previously in anthracene esters.[39]

The progress of the reaction can also be followed using ^{13}C NMR to examine chemical shift changes resulting from the [4+4] photocyclization. In Figure 6 we plot the ^{13}C spectra for 9MA powder after different irradiation times. The loss of aromatic intensity between 120 and 140 ppm is accompanied by the appearance of new sp^3 peaks at 51 and 65 ppm and two new aromatic peaks at 150 ppm. The former derive from the formation of the new bridgehead carbons after the σ bonds form between the anthracene rings, while the latter are assigned to the two benzene carbons at the junction to the nonaromatic central ring. More difficult to discern is the growth of a new dimer methyl peak at 25 ppm, as it is obscured by spinning sidebands; it can easily be observed at other MAS rates, however. The decrease of the monomer methyl peak at 14 ppm can be used as a marker for the amount of monomer remaining, and again we see that even after 240 min of UV exposure, there is still a residual amount of monomer remaining, consistent
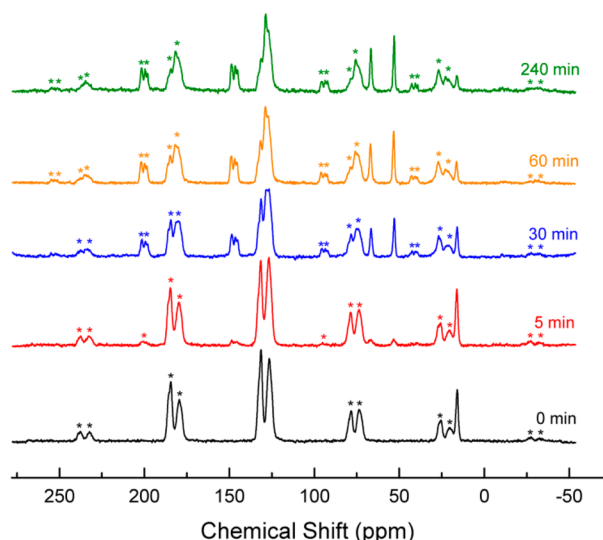
Figure 6. ^{13}C SSNMR data of 9MA microcrystals under UV exposure for 0, 5, 30, 60, and 240 min. Spectra were acquired at 14.1 T and an MAS spin rate of 8 kHz. Spinning side bands are labeled with asterisks. Peak assignments are given in the Supporting Information.

with the PXRD data. No evidence for side products other than the photodimer was observed. The detailed assignment of the peaks in Figure 6 can be found in the Supporting Information.

3. Estimation of Domain Size. Both the PXRD patterns and the ^{13}C SSNMR spectra demonstrate that crystalline 9MA monomer is directly converted into crystalline 9MA dimer, although it appears that this reaction does not proceed to 100% completion. But we must still determine whether it is the simultaneous presence of two phases, crystalline monomer and crystalline dimer, that actually drives the mechanical deformation through the heterometry mechanism. To address this question, we used NMR spin−lattice relaxation experiments to estimate domain sizes. Previous work by Terao and co-workers showed that [1]H T_1 measurements could be used to study the solid-state photodimerization of 9MA.[40] The very different T_1 values of the protons in the monomer and dimer (130 and 17 s, respectively) allow the two species to be distinguished and the extent of their microscopic mixing to be assessed. Facile spin diffusion within the solid means that magnetization recovery for a given proton resonance will reflect the dynamically averaged T_1 of neighboring species.[41−43] In this and the earlier work, the ^{1}H relaxation is indirectly observed by measuring its effect on ^{13}C intensity after cross-polarization. Details of the model, typical magnetization recovery curves, and global fits are given in the Supporting Information. Surprisingly, no significant change in the monomer or photodimer T_1 recoveries were observed at any conversion factor, implying that even from the earliest stages of the reaction the domains are larger than the distance over which spin diffusion is effective. Quantitative analysis of these experiments sets an upper limit for the spin-transfer rate K between domains of $K \leq 5 \times 10^{-3}$ s^{-1}. The inverse of K gives a value $\tau \geq 200$ s for the average time for a spin to traverse a domain. We estimate the spin diffusion coefficient D within a domain using the relation,[44]

$$D = 2r_0^2/T_2 \tag{1}$$

where r_0 is the proton van der Waals radius ($r_0 = 0.117$ nm) and T_2 is the spin−spin relaxation time, measured to be 80 μs

in both the monomer and dimer from the directly observed ^{1}H SSNMR line widths. These values allow us to estimate $D = 340$ nm^2/s. Assuming isotropic diffusion in three dimensions, the average distance covered by the spin during this period is given by

$$R_{domain} = \sqrt{6D\tau} \tag{2}$$

From eq 2, we estimate R_{domain} to be greater than 500 nm, even at the lowest conversion fraction (10%) studied. This was somewhat surprising given that Terao and co-workers resolved changes in K from their T_1 data that suggested smaller domains whose size increased during the course of the reaction.[40] We can only surmise that differences in sample preparation and/or irradiation conditions may account for the discrepancy in T_1 data, since the NMR conditions were very similar. Although our estimate of domain size is fairly rough and involves significant assumptions, the lack of spin exchange between the two domains does indicate the formation of large dimer domains at very early times.

4. Dependence of Crystal Deformation on Reaction Progress. Given that the photodimerization reaction generates a heterogeneous sample with large monomer and dimer domains, how does this provide the energy needed to twist or bend the microscopic crystal? The heterometry mechanism identified by Kahr and co-workers posits that interfacial strain between two crystal phases provides the deformation energy.[45] It should be noted that the data in Figures 5 and 6 were obtained under conditions different (dry powders under less intense radiation for longer times) from those used to induce bending in Figure 4. In order to quantify how the simultaneous presence of reactant and product phases drives crystal deformation, it is necessary to analyze the kinetics of the deformation and the photoreaction in parallel in single microneedles. Recently, low-frequency Raman spectroscopy was used to monitor changes in crystal packing during the course of a photomechanical change.[46] In this work, we rely on fluorescence to monitor the reaction progress. We used a focused 325 nm laser to initiate bending in individual 9MA microneedles while monitoring the fluorescence signal at 550 nm. The face-to-face packing of the 9MA molecules leads to a broad excimer emission peaked at ∼500 nm (Supporting Information). Unlike unsubstituted anthracene crystals, the excimer emission is an intrinsic property of the 9MA crystal and does not require energy migration to defects. The photodimer itself absorbs around 300 nm, below the excitation wavelengths used in these experiments, and does not contribute to the fluorescence signal. Note that there is residual monomer fluorescence at shorter wavelengths that we believe originates from isolated monomers trapped in the dimer matrix. To avoid interference from this weak signal, we detect the fluorescence from the low energy side of the excimer emission at 550 nm to monitor the amount of unreacted monomer pairs left in the illuminated spot.

The rod deformation is quantified by its curvature. The curvature κ is defined as $\kappa = 1/\rho$, where ρ is the radius of a circle which best reproduces the shape of the deformed rod. More details of how ρ is extracted from microscope images of the bending rod are given in the Supporting Information. Figure 7 shows plots of the time-dependent curvature and monomer fluorescence signal for three different needles. In all three examples, the fluorescence signal begins to decay immediately after the light is switched on. There is a time lag of several seconds before bending is observed, after which the
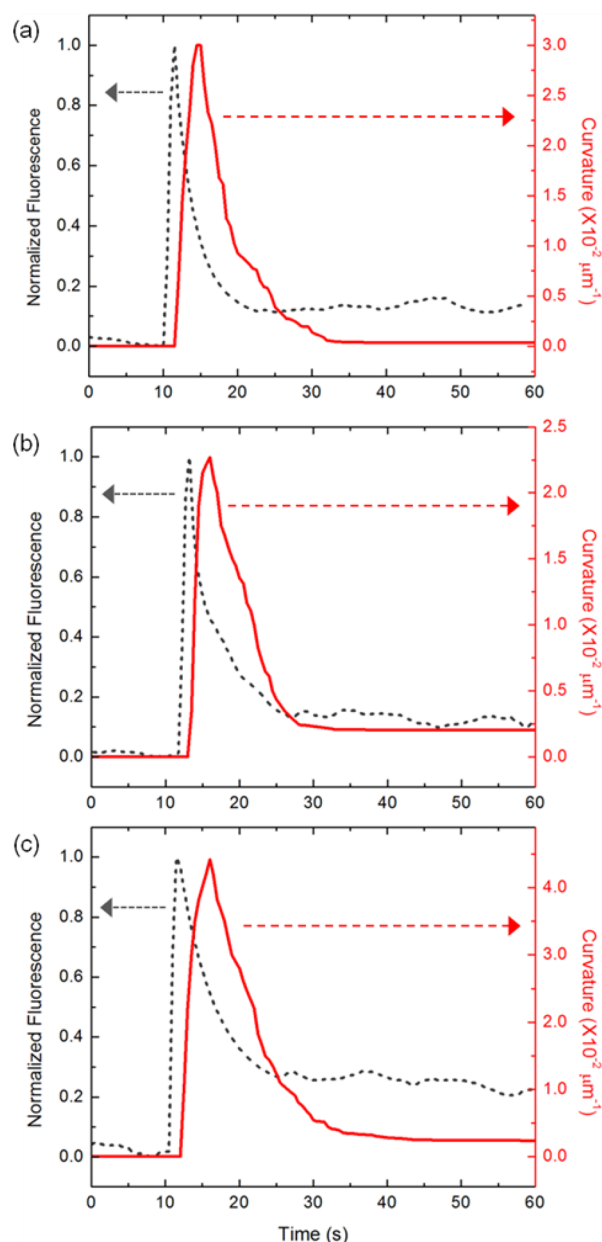
Figure 7. Normalized time-dependent fluorescence and curvature data for three individual 9MA microneedles. In all samples, the peak of the fluorescence signal corresponds to the start of illumination by a focused 325 nm laser spot. The data points are generated by measurement of the monomer fluorescence signal at 550 nm and analysis of fluorescence microscopy images, both collected simultaneously.

curvature quickly jumps to a maximum after the fluorescence signal has decreased by ~50%. After this point, both the curvature and the fluorescence decrease until ~10−20% of the fluorescence signal remains. It does not appear that this residual signal is due to surviving 9MA pairs. From Figure S5 in the Supporting Information, we can see that after a 30 min UV dose, there is still ~20% of the signal remaining at 550 nm in a bulk sample, consistent with our microscopy measurements. But this residual signal can be attributed to the low energy wing of a structured emission peaked at 415 nm that appears as the excimer disappears. We attribute this fluorescence to unreacted monomers trapped in the dimer crystal. It is possible that there

is some excimer contribution as well, but it cannot be discerned under the monomer signal. We note that if the monomer and excimer have similar fluorescence quantum yields, then this remaining signal is consistent with the amount of residual 9MA estimated from the ^{13}C peak intensities. The most important point is that Figure 7 shows that the dynamics of the curvature change and the population conversion are different, and there is no simple relation between the amount of dimer and the amount of curvature.

Finally, we can remove time from the analysis completely and plot the curvature κ versus the dimer fraction f_{dimer}, where f_{dimer} is defined as $f_{dimer} = 1 - f_{mon}$, and f_{mon} is proportional to the normalized fluorescence signal plotted in Figure 7. Figure 8
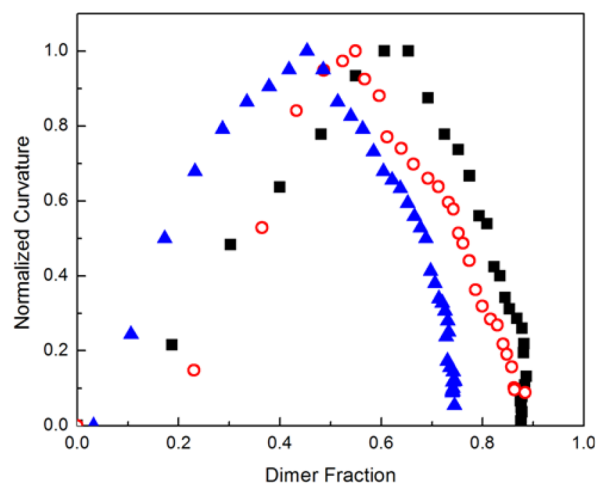

Figure 8. Plot of curvature versus dimer fraction for the three needles whose data are shown in Figure 7, a, black squares; b, red circles; and c, blue triangles.

illustrates this dependence for the three needles shown in Figure 7. We can make several observations concerning these data. First, in all three needles, the curvature has a clear maximum as a function of dimer conversion, but this maximum varies from $f_{dimer} = 0.40$ to $f_{dimer} = 0.65$, depending on the needle studied. As discussed below, the variation in dynamics suggests that the shape change depends sensitively on the details of the needle's initial shape. However, all three needles appear to have a threshold value of $f_{dimer} \approx 0.1$ below which no deformation is observable. Lastly, the dependence of κ on f_{dimer} does not exhibit any obvious discontinuities, as would be expected if the shape change resulted from a phase transition.

■ DISCUSSION

Our work has implications for the design of photomechanical molecular crystals. First, we have shown that it is possible to engineer the type of deformation (e.g., bending or twisting) by controlling the shape of the crystal. Furthermore, we have quantitatively measured how the curvature of a bending microneedle depends on the reaction progress. For the first time, we have shown how the geometrical distortion is related to the relative amounts of reactant and product in a single crystal. A practical outcome of this study is that we have shown that the bending and unbending of such a needle can be accomplished using a single wavelength of light that carries the crystal from a single component reactant (straight) to mixed product/reactant (bent) to single component product (straight again).

In order to better understand the origin of these motions, we now attempt to quantify them using some simple models. Ribbon twisting are the theoretically expected distortion when a layered bimorph structure is created[47] and this was recently characterized experimentally.[16] But the theoretical description of twisting is complicated, so in this paper we only consider the bending in detail. Irie and co-workers have modeled their bending in terms of contraction of one side of the beam while the other side remains constant.[48,49] Simple geometry (Supporting Information) yields an expression for the curvature,

$$\kappa = \frac{1}{\rho} = \frac{1}{w}\frac{1-q}{q} \tag{3}$$

where w is the beam thickness and q is the length ratio of the illuminated side to the non-illuminated side. To obtain a maximum $\kappa = 4 \times 10^{-2}$ μm^{-1} for a beam with $w = 2$ μm, we need a $q \approx 0.93$; i.e., a 7% shrinkage on the dimerized side is required. In 9MA, the monomer and dimer crystals are both monoclinic with similar abc crystal axis orientations relative to the anthracene ring.[31,32] The main result of dimerization is a contraction along the b-axis ($b = 1.4402$ nm for the monomer, $b = 1.3285$ nm for the dimer) accompanied by a slight increase in the c-axis ($c = 0.8026$ nm for the monomer, $c = 0.81301$ for the dimer). If we consider the area defined by the bc plane, it shrinks by ~7% after dimerization, consistent with the maximum observed curvatures in Figure 7. But this simple model cannot describe the growth of dimer domains that determine the intermediate dynamics of bending.

A more sophisticated approach taken by Warner and co-workers is to use elasticity theory to calculate the reduced curvature as a function of strain distribution within the beam.[20] They derive a more complicated expression for the curvature,

$$\kappa \propto \frac{d_{strain}}{w}\left[\left(\frac{d_{strain}}{w} + \frac{1}{2}\right)e^{-w/d_{strain}} - \frac{d_{strain}}{w} + \frac{1}{2}\right] \tag{4}$$

where w is again the beam thickness and d_{strain} is the characteristic exponential decay length of the strain within the beam. We assume that the distribution of products is also exponential, as illustrated in Figure 9a, and characterized by a length, d_{react}. The fraction of dimers is given by

$$f_{dimer} = \frac{d_{react}}{w}(1 - e^{-w/d_{react}}) \tag{5}$$

The relation between d_{react} and d_{strain} is not known, but we assume that they are linearly proportional; i.e., $d_{react} = (constant) \times d_{strain}$. If we assume simple first-order kinetics for the monomer → dimer reaction, we can also derive an expression for f_{dimer} as a function of time (t):

$$f_{dimer} = 1 - e^{-kt} \tag{6}$$

where k is the photochemical reaction rate. Equations 4−6 provide a way to connect κ (the bending), f_{dimer}, and t. The calculated time evolution of the monomer population is shown in Figure 9b ($k = 0.1$ s^{-1}), along with two calculated $\kappa(t)$ curves for $d_{react} = d_{strain}$ and $d_{react} = 2d_{strain}$ We set $w = 2$ μm to be consistent with the needle diameters seen in Figure 2a. It can be seen that the $d_{react} = 2d_{strain}$ curve peaks later and is broader than the $d_{react} = d_{strain}$ curve. In Figure 9c, we plot two calculated κ curves as a function of f_{dimer}. For $d_{react} = d_{strain}$, the maximum occurs at $f_{dimer} = 0.345$, earlier than what is observed
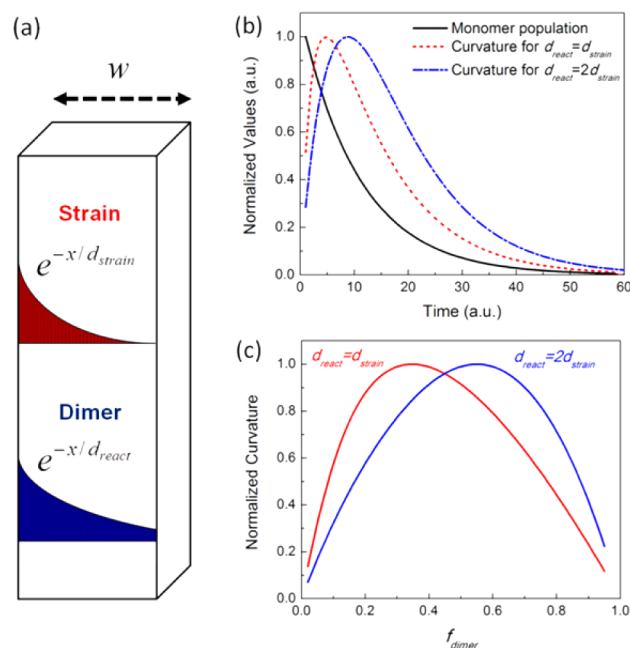

Figure 9. (a) Diagram of strain and dimer distribution inside the beam with thickness of w. (b) Calculated monomer population (solid black) and curvature of beam against time when $d_{react} = d_{strain}$ (dotted red) and $2d_{strain}$ (dash-dotted blue). (c) Calculated curvature against dimer fraction, f_{dimer}.

experimentally. For $d_{react} = 2d_{strain}$, the maximum occurs at $f_{dimer} = 0.548$, a value which agrees more closely with the experimental curves in Figure 8. Considering the variation in dynamics between different bending data in Figures 7 and 8, we cannot assign a definite value for the proportionality constant that relates d_{react} to d_{strain}. But if these characteristic lengths were more than a factor of 2 different, our calculations suggest that we would be able to see this difference in the data. These results show that the dynamics of the bending motion are consistent with the evolution of a strain gradient within the needle due to the preferential growth of dimer domains on one side, and that the strain follows the distribution of dimers closely (to within a factor of 2).

Both the maximum curvature and the dynamics of the bending in the microneedles are consistent with the bimorph mechanism. This is the same result that would be expected if we had illuminated only one side of the crystal to generate a normal bimorph structure. The interesting thing is that this bimorph type motion is induced by the non-directional lamp illumination. How can uniform illumination lead to this asymmetry? Put another way, if the dimer simply nucleates at random defects uniformly distributed throughout the crystal,[40] how can this induce the anisotropic motion analyzed above? We consider three possible mechanisms. One explanation is that on the microscopic scale, the illumination is not really homogeneous. The edges and orientation of the crystal necessarily block some light, and one side will receive more than the other. This imbalanced illumination, due to the details of the microstructure, may generate locally asymmetric illumination conditions, in much the same way that shining a laser from one side would. A second mechanism centers on the asymmetric absorption properties of the crystal lead to preferential absorption along one side. In 9MA, as in unsubstituted anthracene, the transition dipole moment (TDM) lies along the short axis of the anthracene ring.

Given the molecular orientations shown in Figure 3b, one would expect that light impinging from the top would be preferentially absorbed, since its direction of propagation is perpendicular to the TDM in all cases. Light incident from the side, on the other hand, will see less absorption due to the fact that some anthracene rings can be oriented such that they cannot couple to the electric field. The effective absorption coefficient of different crystal faces can vary by an order of magnitude, and this could also lead to an asymmetric buildup of product on one side of the microcrystal. A third possibility is that distinct reactant and product spatial domains spontaneously form as a result of the intrinsic solid-state reaction dynamics, rather than as the result of special illumination conditions. Several solid-state photodimerizations are known to proceed in a heterogeneous fashion with strong deviations from simple first-order kinetics.[50−52] Mabied et al. provided evidence that the solid-state 9MA photodimerization kinetics are consistent with a nucleation and growth process.[32] In other words, the presence of dimers in the monomer crystal facilitates the formation of additional dimers. If the first dimers are formed at the crystal surface due to steric constraints, then a bimorph structure would be the inevitable outcome of the solid-state reaction kinetics, regardless of reaction conditions. Some support for such a mechanism in our crystals comes from our SSNMR measurements, which show that large (>500 nm) domains form very early in the photoreaction, even after just 10% conversion.

In reality, all three of the above mechanisms may be contributing to the directional bending under uniform illumination. Since the first two rely on differential absorption, it should be possible to test for them by varying either the excitation wavelength or the crystal thickness. By choosing a longer wavelength or by making the crystal sufficiently thin, we should be able to bring about a situation where the absorption of the exciting light is uniform across the crystal (i.e., $d \gg w$ in eq 4). Experiments to test the dependence of the photomechanical response on wavelength and crystal dimensions are currently underway. In order to test whether the reaction kinetics provide an intrinsic mechanism for the generation of a bimorph structure, we need to perform experiments that map out the spatial distribution of reactant and product molecules within a single microcrystal. Since these domains are expected to be sub-micrometer, it will be challenge to resolve them using optical microscopy, although we are currently attempting such experiments.

While the detailed mechanism of the asymmetric motion remains a subject of investigation, our results show that the motion can be precisely controlled by the amount of photodimer produced. In the case of 9MA the motion depends on the amount of light exposure, since if the reaction goes to completion, the needle or ribbon returns to its original shape as the crystal becomes predominantly single domain, i.e., the photoproduct. Although it is straightforward to control the duration of light exposure, this still places a limitation on the robustness of the photomechanical response. A considerable fraction (10−20%) of 9MA monomers do not react in our crystals, but this level of monomer is apparently not enough to maintain the physical deformation seen at intermediate times. The reason that the 9MA photdimerization does not go to completion in our crystals is not clear. In contrast to 9AC, the monomers are paired within the 9MA crystal, and there is no statistical reason why they should not all react with each other. It may be that during the reaction, the formation of dimer regions leads to distortions or defects in the remaining monomer crystal that break up some 9MA pairs before they can react.

Finally, given that f_{dimer} controls the amount of mechanical distortion, we should mention that there exist other ways to control this parameter besides controlling the amount of light exposure. It is possible for the crystal structure itself to limit the reaction yield. An example is the one-dimensional stacking of 9AC molecules that places a statistical limit on the dimerization yield.[24,26] For this material, a given crystal always twists the same amount, regardless of the amount of light exposure. Another strategy would rely on photophysics rather than crystal engineering. If the reactants and products have overlapping absorption spectra, a well-chosen excitation wavelength can generate a photostationary state where both reactants and products coexist in equilibrium.[53]

■ CONCLUSION

In this Article, we have used a prototypical solid-state reaction, the photodimerization of 9MA, to investigate how crystal morphology and solid-state reaction dynamics combine to generate photomechanical deformations of single crystals. By varying the crystallization conditions, we were able to prepare both microneedles and microribbons of 9MA. The different shapes showed different types of motion, bending versus twisting, under irradiation. In both crystal shapes the maximum deformation occurs at roughly the midpoint of the reaction, rather than at its completion. Analysis of the NMR spin−lattice relaxation measurements is consistent with the formation of monomer and dimer crystal domains. In the microneedles, both the dynamics and the magnitude of the bending are consistent with the formation of a bimorph structure within the needle. These observations provide clear evidence for the heterometry mechanism for the mechanical response. The results of this work demonstrate that both crystal morphology and reaction kinetics must be considered in order to design a structure with a well-defined photomechanical response. The rational design of molecular crystal photomechanical elements is a complex problem, but its solution could lead to nanoscale actuators that can be controlled remotely by light.

■ ASSOCIATED CONTENT

Ⓢ Supporting Information

SEM determination of ribbon and needle cross sections; measurement of needle bend radius during illumination in an optical microscope; ^{13}C SSNMR peak assignments; spin-exchange modeling of ^{1}H T_1 relaxation rates; absorption and fluorescence of 9MA in the solid state; two-dimensional models for domain growth and time-dependent interfacial area. This material is available free of charge via the Internet at http://pubs.acs.org.

■ AUTHOR INFORMATION

Corresponding Author

christopher.bardeen@ucr.edu

Notes

The authors declare no competing financial interest.

■ ACKNOWLEDGMENTS

■ REFERENCES

(1) McBride, J. M.; Segmuller, B. E.; Hollingsworth, M. D.; Mills, D. E.; Weber, B. A. *Science* **1986**, *234*, 830−835.

(2) Luty, T.; Eckhardt, C. J. *J. Am. Chem. Soc.* **1995**, *117*, 2441−2452.

(3) MacGillivray, L. R.; Papaefstathiou, G. S.; Friscic, T.; Hamilton, T. D.; Bucar, D. K.; Chu, Q.; Varshney, D. B.; Georgiev, I. G. *Acc. Chem. Res.* **2008**, *41*, 280−291.

(4) Cohen, M. D. *Angew. Chem., Int. Ed.* **1975**, *14*, 386−393.

(5) Schmidt, G. M. J.; Cohen, M. D.; Donitz, J. D.; Hammond, C. S. *Solid-state photochemistry*; Verlag Chemie: Germany, 1976.

(6) Keating, A. E.; Garcia-Garibay, M. A., Photochemical solid-to-solid reactions. In *Organic and Inorganic Photochemistry*, 1st ed.; Ramamurthy, V., Schanze, K. S., Eds.; Dekker: New York, 1998; Vol. 2, pp 195−248.

(7) Al-Kaysi, R. O.; Muller, A. M.; Bardeen, C. J. *J. Am. Chem. Soc.* **2006**, *128*, 15938−15939.

(8) Al-Kaysi, R. O.; Bardeen, C. J. *Adv. Mater.* **2007**, *19*, 1276−1280.

(9) Garcia-Garibay, M. A. *Angew. Chem., Int. Ed.* **2007**, *46*, 8945−8947.

(10) Uchida, K.; Sukata, S.; Matsuzawa, Y.; Akazawa, M.; de Jong, J. J. D.; Katsonis, N.; Kojima, Y.; Nakamura, S.; Areephong, J.; Meetsma, A.; Feringa, B. L. *Chem. Commun.* **2008**, 326−328.

(11) Koshima, H.; Ojima, N.; Uchimoto, H. *J. Am. Chem. Soc.* **2009**, *131*, 6890−6891.

(12) Naumov, P.; Kowalik, J.; Solntsev, K. M.; Baldridge, A.; Moon, J.-S.; Kranz, C.; Tolbert, L. M. *J. Am. Chem. Soc.* **2010**, *132*, 5845−5857.

(13) Koshima, H.; Nakaya, H.; Uchimoto, H.; Ojima, N. *Chem. Lett.* **2012**, *41*, 107−109.

(14) Koshima, H.; Takechi, K.; Uchimoto, H.; Shiro, M.; Hashizume, D. *Chem. Commun.* **2011**, *47*, 11423−11425.

(15) Naumov, P.; Sahoo, S. C.; Zakharov, B. Z.; Boldyreva, E. V. *Angew. Chem., Int. Ed.* **2013**, *52*, 9990−9995.

(16) Kitagawa, D.; Nishi, H.; Kobatake, S. *Angew. Chem., Int. Ed.* **2013**, *52*, 9320−9322.

(17) Sun, J.-K.; Li, W.; Chen, C.; Ren, C.-X.; Pan, D.-M.; Zhang, J. *Angew. Chem., Int. Ed.* **2013**, *52*, 6653−6657.

(18) Kobatake, S.; Takami, S.; Muto, H.; Ishikawa, T.; Irie, M. *Nature* **2007**, *446*, 778−781.

(19) Morimoto, M.; Irie, M. *J. Am. Chem. Soc.* **2010**, *132*, 14172−14178.

(20) Warner, M. *Phys. Rev. Lett.* **2004**, *92*, 134302/1−134302/4.

(21) Ikeda, T.; Mamiya, J.; Yu, Y. *Angew. Chem., Int. Ed.* **2007**, *46*, 506−528.

(22) Takahashi, S.; Miura, H.; Kasai, H.; Okada, S.; Oikawa, H.; Nakanishi, H. *J. Am. Chem. Soc.* **2002**, *124*, 10944−10945.

(23) Bucar, D. K.; MacGillivray, L. R. *J. Am. Chem. Soc.* **2007**, *129*, 32−33.

(24) Zhu, L.; Al-Kaysi, R. O.; Bardeen, C. J. *J. Am. Chem. Soc.* **2011**, *133*, 12569−12575.

(25) Kim, T.; Zhu, L.; Mueller, L. J.; Bardeen, C. J. *CrystEngComm* **2012**, *14*, 7792−7799.

(26) Cohen, E. R.; Reiss, H. *J. Chem. Phys.* **1963**, *38*, 680−691.

(27) Birks, J. B.; Aladekomo, J. B. *Photochem. Photobiol.* **1963**, *2*, 415−418.

(28) Heller, E.; Schmidt, G. M. J. *Isr. J. Chem.* **1971**, *9*, 449−462.

(29) Ferguson, J.; Miller, S. E. H. *Chem. Phys. Lett.* **1975**, *36*, 635−638.

(30) Kaupp, G. *Angew. Chem., Int. Ed.* **1992**, *31*, 595−598.

(31) Turowska-Tyrk, I.; Trzop, E. *Acta Crystallogr. B* **2003**, *59*, 779−786.

(32) Mabied, A. F.; Muller, M.; Dinnebier, R. E.; Nozawa, S.; Hoshino, M.; Tomita, A.; Sato, T.; Adachi, S. *Acta Crystallogr. B* **2012**, *68*, 424−430.

(33) Yamamoto, S.; Grellmann, K. H.; Weller, A. *Chem. Phys. Lett.* **1980**, *70*, 241−245.

(34) Ebeid, E. Z. M.; Habib, A. F. M.; Azim, S. A. *React. Solids* **1988**, *6*, 39−44.

(35) Dvornikov, A. S.; Rentzepis, P. M. *Res. Chem. Intermed.* **1996**, *22*, 115−128.

(36) Funk, B. K.; Khitrin, A. K.; Ermolaev, K. *J. Magn. Reson.* **2000**, *142*, 97−101.

(37) Zhu, L.; Al-Kaysi, R. O.; Dillon, R. J.; Tham, F. S.; Bardeen, C. J. *Cryst. Growth Des.* **2011**, *11*, 4975−4983.

(38) Campione, M.; Ruggerone, R.; Tavazzi, S.; Moret, M. *J. Mater. Chem.* **2005**, *15*, 2437−2443.

(39) Zhu, L.; Agarwal, A.; Lai, J.; Al-Kaysi, R. O.; Tham, F. S.; Ghaddar, T.; Mueller, L.; Bardeen, C. J. *J. Mater. Chem.* **2011**, *21*, 6258−6268.

(40) Takegoshi, K.; Nakamura, S.; Terao, T. *Solid State Nucl. Magn. Reson.* **1998**, *11*, 189−196.

(41) Clauss, J.; Schmidt-Rohr, K.; Spiess, H. W. *Acta Polym.* **1993**, *44*, 1−17.

(42) Demco, D. E.; Johansson, A.; Tegenfeldt, J. *Solid State Nucl. Magn. Reson.* **1995**, *4*, 13−38.

(43) VanderHart, D. L.; McFadden, G. B. *Solid State Nucl. Magn. Reson.* **1996**, *7*, 45−66.

(44) Assink, R. A. *Macromolecules* **1978**, *11*, 1233−1237.

(45) Shtukenberg, A. G.; Freudenthal, J.; Kahr, B. *J. Am. Chem. Soc.* **2010**, *132*, 9341−9349.

(46) Salzillo, T.; Bilotti, I.; Valle, R. G. D.; Venuti, E.; Brillante, A. *J. Am. Chem. Soc.* **2012**, *134*, 17671−17679.

(47) Chen, Z.; Majidi, C.; Srolovitz, D. J.; Haataja, M. *Appl. Phys. Lett.* **2011**, *98*, 011906/1−011906/3.

(48) Kuroki, L.; Takami, S.; Yoza, K.; Morimoto, M.; Irie, M. *Photochem. Photobiol. Sci.* **2010**, *9*, 221−225.

(49) Terao, F.; Morimoto, M.; Irie, M. *Angew. Chem., Int. Ed.* **2012**, *51*, 901−904.

(50) Bertmer, M.; Nieuwendaal, R. C.; Barnes, A. B.; Hayes, S. E. *J. Phys. Chem. B* **2006**, *110*, 6270−6273.

(51) Benedict, J. B.; Coppens, P. *J. Phys. Chem. A* **2009**, *113*, 3116−3120.

(52) More, R.; Busse, G.; Hallmann, J.; Paulmann, C.; Scholz, M.; Techert, S. *J. Phys. Chem. C* **2010**, *114*, 4142−4148.

(53) Zheng, S. L.; Messerschmidt, M.; Coppens, P. *Chem. Commun.* **2007**, 2735−2737.